LBNL-39609
UC-413
Preprint

ERNEST ORLANDO LAWRENCE
BERKELEY NATIONAL LABORATORY

α-Particle Induced γ-Ray Transitions in Light Elements

R.K. Heaton, H.W. Lee, B.C. Robertson,
E.B. Norman, K.T. Lesko, and B. Sur
Nuclear Science Division

October 1996
Submitted to
Physical Review C

LBNL-39609
UC-413

α-Particle Induced γ-Ray Transitions in Light Elements

R.K. Heaton, H.W. Lee, and B.C. Robertson

Department of Physics
Queen's University
Kingston, Canada K7L 3N6

E.B. Norman, K.T. Lesko, and B. Sur

Nuclear Science Division
Ernest Orlando Lawrence Berkeley National Laboratory
University of California
Berkeley, California 94720

October 1996

This work was supported in part by a grant from NSERC and by the U.S. Department of Energy under Contract No. DE-AC03-76SF00098.

α-Particle Induced γ-Ray Transitions in Light Elements *

R. K. Heaton†, H. W. Lee, B. C. Robertson

Department of Physics, Queen's University,
Kingston, Canada K7L 3N6

E. B. Norman, K. T. Lesko, B. Sur‡

Nuclear Science Division, Lawrence Berkeley National Laboratory,
Berkeley, California 94720

October 7, 1996

Abstract

The absolute γ-ray yields from α-particle-induced reactions on thick targets of Be, BN, NaF, Mg, Aℓ and Si for incident energies between 5.6 and 10 MeV are presented. The excitation distributions of several nuclei have been deduced from the experimental γ-ray yields and are compared to theoretical predictions based on a statistical model of nuclear reactions.

1 Introduction

Statistical nuclear reaction models have produced reaction cross sections which agree within a factor of two with experimental measurements for medium and heavy nuclei. Reaction cross sections known to this level of accuracy are useful in γ-ray background calculations for ultra-low background experiments, where backgrounds are dominated by the intrinsic radioactivity of the laboratory and detector materials. These backgrounds result from both the primary decay spectrum associated with natural radioactivity and from secondary reactions induced by energetic decay products, mostly α-particles. The γ-ray background from the primary decay component is known to be small above 4 MeV, so that secondary reactions become more significant. The magnitudes of these secondary reactions are largely dominated by Coulomb barrier penetration, and therefore are sensitive to the presence of light elements. Few experimental measurements for light elements are available in the energy range of α-particles from the uranium and thorium chains, so background predictions have to rely largely on theoretical calculations. In this work, the applicability of statistical model calculations to light elements is investigated by comparison to a set of experimentally measured thick target γ-ray yields.

The following section describes the experiment and analytical techniques used to obtain thick-target γ-ray yields in Be, B, F, Na, Aℓ, Mg and Si. This is followed by a presentation and discussion of the experimental results. Theoretical yields based on the statistical model are described in Section 4, and compared with experimental results in Section 5. The level of agreement obtained following different simplifying approximations is examined for several nuclear reactions. The accuracy of these theoretical calculations is further explored through a comparison of γ-ray energy distributions based on experimental measurements and theoretical calculations.

2 Experiment

The measurement and calculation techniques used in this study are outlined below; a detailed description has been published previously [1]. Measurements of the thick-target γ-ray yields were performed using Lawrence

*The authors would like to thank Dr. Ian Towner for providing the computer code DSTWAV used in this study. This work was supported in part by a grant from NSERC and in part by the U.S. Department of Energy under contract #DE-AC03-76SF00098.

†Present address: London Regional Cancer Centre, 790 Commissioners Road East, London, Canada N6A 4L6.

‡Present address: Chalk River Nuclear Laboratories, Chalk River, Canada K0J 1J0.

Berkeley National Laboratory's 88″ cyclotron. Thick targets of Be, BN, NaF, Mg and Aℓ were exposed to α-particle beams with energies of 10, 8.8, 7.7, 7.0, 6.3 and 5.6 MeV, while a target of Si was exposed to 10 MeV α-particles only.

The resulting γ-rays were detected in 100 cm^3 hyper-pure germanium detectors placed at 30.6° and 109.9° with respect to the α-particle beam. Spectra between 2 and 10 MeV were recorded. An annotated portion of each γ-ray spectrum from the 109.9° detector for the highest energy α-particle beam is shown in Fig 1. A pulser signal triggered by the target current integrator was injected into the high-energy portion of each spectrum to monitor the detector live time. The low energy γ-ray rate was reduced by placing a 2 cm thick lead attenuator in front of each detector.

The area of each γ-ray peak, obtained by subtracting the underlying background determined from a quadratic fit to surrounding regions, was normalized to the α-particle counts on target, the detector efficiency and the detector live time. The corresponding absolute γ-ray yield was extracted from the γ-ray distribution by a fit of the two normalized peak areas to the zeroth and second order Legendre polynomials; higher order contributions were minimized by positioning the detectors near the zeros of the fourth and sixth order terms in the expansion.

Both statistical and systematic uncertainties were incorporated into the calculation of the transition yields. Statistical uncertainties included those from the counts in a peak area, the live time and detector efficiency. Additional systematic uncertainties were evaluated for the extrapolation of the background beneath the peak as well as for the detector efficiency and live time. A further uncertainty was added to the $E_\alpha = 8.8$ MeV measurements to account for a loss of beam resulting from degraded beam focus at this energy. Statistical uncertainties were propagated in quadrature, while systematic uncertainties were propagated linearly. The statistical and systematic uncertainties were assumed to be independent, and were combined in quadrature.

3 γ-Ray Yields

Tables 1 through 14 report the measured thick-target reaction yields per α-particle for the equivalent elementally pure targets containing natural isotopic abundances. The yields in these tables have been listed in a condensed form with the number and error followed by the power of 10 in brackets. For example, an entry of $4.3 \pm 1.2(-7)$ indicates a yield of $(4.3 \pm 1.2) \times 10^{-7}$ γ-rays per α.

Only yields which could be assigned uniquely to a residual nucleus are reported. Spectral peaks containing multiple transitions contributing more than 5% to the total peak area were separated into constituent yields using published decay schemes [2, 3, 4]. The population of each contributing level was determined from the γ-ray intensity of alternate decay branches from the level, and then used to calculate the contribution to the composite yield. The contribution was subtracted from the yield, enabling the determination of all yield components. In cases where this subtraction resulted in unreasonable uncertainties in a weak yield branch (<20% of total yield), the total statistical uncertainty was calculated from the quadrature sum of level population and branching ratio uncertainties. Such cases are marked next to the affected yield entry, or next to the transition identification when all yields were affected.

A number of adjustments were applied to the yields. In a few cases kinematic peak broadening caused an overlap of transitions resulting in ambiguous identifications which could not be resolved using the known level populations. Cases in which the majority of the yield could be attributed to a single transition on the basis of average level populations of residual nuclei are reported with an uncertainty increased to equal the estimated contamination. These yields are marked in the tables as containing additional contaminations.

The interaction of neutrons from the (α, n) reaction also necessitated some yield adjustments. The 2614 keV γ-ray from neutron and α-particle scattering on ^{208}Pb in the lead attenuators produced a sharp peak, while the iron 7631/7647 keV neutron capture doublet [5] produced a broader peak. All neutron-induced peak areas were found to scale with the calculated neutron yield determined from published tables [6]. Neutron effects were determined by isolating the induced peaks or by using the observed scaling with neutron yield.

A number of yields were obtained through additional analysis which resulted in larger uncertainties, while some ambiguous transitions were excluded from the tables altogether. Such transitions are discussed below, along with estimates of their yields and uncertainties.

A broad peak in the BN target spectrum near 2140 keV attributed to inelastic scattering off both ^{10}B and ^{11}B was excluded from the tables. This peak was present at all measured energies, and had yields for elemental boron ranging from 1.89×10^{-5} γ-rays per α at $E_\alpha = 10$ MeV to 7.41×10^{-8} γ-rays per α at $E_\alpha = 5.6$ MeV.

The NaF target peak at 3880 keV, attributed to both the ^{23}Na$(\alpha,n)^{26}$Mg 5690 $\rightarrow$ 1809 keV and ^{19}F$(\alpha,p)^{22}$Ne 5147 $\rightarrow$ 1274 keV transition, was excluded. The target yield for this peak ranged from 1×10^{-6} γ-rays per α-particle at 10 MeV to 2×10^{-7} at 7 MeV. The 2130 keV peak in the NaF target also was excluded. Both the ^{23}Na$(\alpha,n)^{26}$Aℓ 2545 $\rightarrow$ 417 keV and the ^{23}Na$(\alpha,p)^{26}$Mg 3941 $\rightarrow$ 1809 keV transitions could equally contribute to the yield. A target yield of between 3.62×10^{-8} and 1.3×10^{-6} γ-rays per α from this transition was observed between α-particle energies of 5.6 and 10 MeV.

In the Mg target, a peak at 3936 keV attributed to the ^{25}Mg$(\alpha,p)^{28}$Aℓ 3936 $\rightarrow$ 0 keV and ^{26}Mg$(\alpha,p)^{29}$Aℓ 3935 $\rightarrow$ 0 keV transitions was excluded from the tables. This peak was observed at $E_\alpha = 10$ through 7.7 MeV with a yield of 4.98×10^{-7} to 4.01×10^{-8} γ-rays per α, respectively. A peak at 3255 keV attributed to the ^{25}Mg$(\alpha,p)^{28}$Aℓ 3296 $\rightarrow$ 31 keV and ^{26}Mg$(\alpha,n)^{29}$Si 5285 $\rightarrow$ 2028 keV transitions observed at energies of 10 MeV through 7.0 MeV, with yields ranging between 3.15×10^{-7} and 1.90×10^{-8} γ-rays per α was also excluded. Due to the relatively few γ-rays observed for the ^{25}Mg(α,p) reaction, these two exclusions may account for as much as half the γ-ray intensity from the ^{28}Aℓ residual nucleus.

Only a few uniquely determined (α,α') transitions were identified. The ^{19}F(α,α') 2780 $\rightarrow$ 197 keV transition had measured yields of $(2.48 \pm 0.14) \cdot 10^{-8}$, $(6.64 \pm 0.93) \cdot 10^{-6}$, and $(3.58 \pm 0.22) \cdot 10^{-6}$ γ-rays per α at $E_\alpha =$ 10, 8.8 and 7.7 MeV, respectively. The ^{25}Mg(α,α') 2738 $\rightarrow$ 0 and ^{27}A$\ell(\alpha,\alpha')$ 3680 $\rightarrow$ 844 keV transition yield for $E_\alpha = 10$ MeV was $(1.65 \pm 0.41) \cdot 10^{-6}$ and $(6.18 \pm 2.31) \cdot 10^{-7}$ γ-rays per α respectively.

No table has been provided for the single 4439 keV γ-ray observed from Be. Be yields reported previously [1] are due to this transition alone, and are not repeated here.

Only two excitations were observed for the ^{11}B$(\alpha,p)^{14}$C reaction, and both of these occurred only for $E_\alpha =$ 10 MeV. At this α-particle energy, the 6728 $\rightarrow$ 0 keV yield was $(2.64 \pm 0.27) \cdot 10^{-7}$ γ-rays per α and the 6094 $\rightarrow$ 0 keV yield was $(1.07 \pm 0.06) \cdot 10^{-6}$ γ-rays per α.

Only the 4439 $\rightarrow$ 0 keV transition γ-ray was observed from the ^{10}B$(\alpha,d)^{12}$C reaction. The transition yields were $(1.11 \pm 0.08) \cdot 10^{-5}$, $(2.09 \pm 0.29) \cdot 10^{-6}$, $(1.06 \pm 0.05) \cdot 10^{-6}$, $(6.00 \pm 0.44) \cdot 10^{-7}$, $(1.77 \pm 0.09) \cdot 10^{-7}$, $(4.97 \pm 0.49) \cdot 10^{-8}$ γ-rays per α for $E_\alpha =$ 10, 8.8, 7.7, 7.0, 6.3 and 5.6 MeV, respectively.

Contamination of the 2313 keV level from the ^{11}B$(\alpha,n)^{14}$N reaction by the ^{14}N(α,α') reaction was accounted for using inelastic scattering cross sections reported by Dyer *et al.* [7]. The (α,α') thick-target yield per α for this γ-ray was 3.01×10^{-6} at $E_\alpha = 10$ MeV, 9.12×10^{-7} at $E_\alpha = 8.8$ MeV, and 1.06×10^{-7} at $E_\alpha = 7.7$ MeV, respectively, with associated uncertainties of 10%. At 10 MeV, the (α,α') reaction accounted for 13% of the combined yield, and at 7.7 MeV accounted for less than 3%.

Only two ^{14}N$(\alpha,p)^{17}$O transition yields were determined in this study. The 3841 $\rightarrow$ 0 keV transition had measured yield intensities at $E_\alpha = 10$ and 8.8 MeV of $(4.71 \pm 0.22) \cdot 10^{-6}$ and $(1.35 \pm 0.36) \cdot 10^{-7}$ γ-rays per α, respectively, and the 3055 $\rightarrow$ 871 keV transition had measured yield at $E_\alpha = 10$, 8.8 and 7.7 MeV of $(2.09 \pm 0.38) \cdot 10^{-6}$, $(5.22 \pm 1.03) \cdot 10^{-7}$ and $(2.42 \pm 0.18) \cdot 10^{-7}$ γ-rays per α, respectively.

The ^{19}F$(\alpha,p)^{22}$Ne 6115 $\rightarrow$ 1274 keV transition was contaminated by the ^{23}Na$(\alpha,n)^{26}$Mg 4834 $\rightarrow$ 0 keV transition at $E_\alpha = 10$ and 8.8 MeV, conservatively estimated at 20% from neighboring level populations and lower α-particle energy behavior. The total yield at these energies has been attributed to the 6115 $\rightarrow$ 1274 keV transition, with an additional 20% uncertainty. No yield for the 4834 $\rightarrow$ 0 keV transition in the 10 and 8.8 MeV E_α runs has been assigned, while at lower energies reaction kinematics permitted both transitions to be resolved.

The ^{19}F$(\alpha,n)^{22}$Na 3519 $\rightarrow$ 0 keV yield was separated from the ^{23}Na$(\alpha,n)^{26}$Aℓ 3508 $\rightarrow$ 0 keV yield using level lifetime information. The 3519 keV level in ^{22}Na has a lifetime of 0.6 ps, which is also the same order as the stopping time (0.5 ps [8]) for an ion in the target, while the 3508 keV level in ^{26}Aℓ has a much shorter lifetime of 0.02 fs. The sharp, fully Doppler-shifted 3508 keV γ-ray peak on top of the extended broad 3519 keV peak was isolated and subtracted from the total area. An additional uncertainty of 20% was assigned to both yields to reflect the observed area ratio fluctuation between detectors.

This procedure was also used to separate the sharp peak of the long lived ^{19}F$(\alpha,n)^{22}$Na 2571 $\rightarrow$ 0 keV transition from the broad ^{19}F(α,α') 2780 $\rightarrow$ 197 keV transition. Again, an area ratio fluctuation contributed an additional 20% uncertainty to these yield determinations.

In the forward angle detector of the $E_\alpha = 10$ MeV run, the ^{23}Na$(\alpha,p)^{26}$Mg 5715 $\rightarrow$ 2938 keV transition was contaminated by the pulser peak. The separation of pulser and transition areas resulted in a large statistical uncertainty of 85% for the forward detector γ-ray peak area.

The level branching ratios determined from these yields are in agreement with published values [2, 3, 4] within statistical uncertainty, with the sole exception being the decay of the 4895 keV level from the ^{26}Mg$(\alpha,p)^{29}$Si reaction. The published branching ratios indicate that transitions to the ground state and first excited state decay

in a ratio of 1:3.1, with a 16% uncertainty. The measurements reported here indicate a stronger ground state transition leading to ratios between 1:1.6 to 1:0.82, and exclude the published value at the 1σ level of statistical uncertainty (20%). This behavior was attributed to some unidentified contamination of the weak ground state transition.

4 Statistical Nuclear Reaction Calculations

The results presented above allow an evaluation of statistical nuclear reaction models for these light nuclei. Statistical compound nuclear model reaction cross sections have been calculated and integrated with stopping powers [9] to provide estimates of the thick-target yield for excitations of the residual nucleus, which were compared to experimental values.

The statistical model of nuclear reactions is based on the assumption that all reactions proceed via the formation of a compound nucleus which then decays through all energetically possible channels. The excitation of the compound nucleus is assumed to be such that individual levels strongly overlap so that the decay is independent of the detailed level structure. The reaction cross sections calculation separates into two steps: the calculation of the cross section for forming the compound nucleus, and the calculation of the branching ratios for the decay of the nucleus by the various channels. The absorption cross section is typically obtained from solutions of the optical potential for the appropriate incident particle. The channel decay probability can be found by combining absorption cross sections and the density of nuclear states using the principle of detailed balance to obtain the inverse absorption cross section from these components. Through an extension of this principle, the excitation probability of a particular energy region in the residual nuclei was estimated.

Two types of absorption cross section sources were used in this study. The first source was a parameterization of optical model total absorption cross section results [10, 11, 12] by Chatterjee, Murphy and Gupta [13]. The second source was derived from distorted-wave Born approximation (DWBA) solutions of the wavefunction provided by the Oxford computer code DSTWAV [14] using two different parameterizations of the optical potential. One set of potentials was taken from global parameterizations where the potential was treated as a smooth function of atomic number, mass and particle energy; the other set was derived from parameters obtained from phenomenological fits to experimental data for individual nuclei[15]. Both types of potential were used in statistical model calculations to provide a detailed comparison with experimental results for the $^{25}\mathrm{Mg}(\alpha,n)^{28}\mathrm{Si}$, $^{26}\mathrm{Mg}(\alpha,n)^{29}\mathrm{Si}$, and $^{27}\mathrm{A}\ell(\alpha,p)^{30}\mathrm{Si}$ reactions.

4.1 Optical Potentials

A number of studies have established global optical potential parameters for neutrons and protons. The most recent studies by Becchetti and Greenlees [16] and Varner, Clegg, McAbee and Thompson [17] indicate a dependence of the potential depths on both particle energy and nuclear isospin for nuclei with mass numbers of 40 and greater. Below this mass range, and at low incident energies, non-systematic nuclear structure effects cause departures from this smooth behavior and complicate the use of a global parameterization for these nuclei.

Some global parameterizations applicable to the low energy and medium mass range have been developed. In this investigation, a potential presented in a study of medium mass nuclei by Alexander *et al.* [18] was used, to which the spin-orbit potential of Varner *et al.* [17] was added. The global parameterization for low energy protons suggested by Perey and Perey [15, 19] and applicable down to a mass number of ~30 was used. Both potentials were derived from the scattering data tabulated in [15].

Although many investigations have attempted to parameterize the optical potential for α-particles, consistent systematic potentials have not been found [15]. The low energy behavior has not been well established due to the predominance of Coulomb scattering below 20 MeV. McFadden and Satchler [20] were unable to find a reasonable mass parameterization of the potential in their study of 24.7 MeV α-particles for elements ranging from oxygen to uranium. In the present study, the average values suggested by McFadden and Satchler were used for all nuclei, and no energy dependence has been introduced in the potential parameters.

Phenomenological potentials [15] were linearly extrapolated to unstable nuclei using the isospin dependence of Varner. The energy dependence of Varner also was added to both neutron and proton potentials. No isospin extrapolation or energy dependence was used in determining the phenomenological α-particle potentials.

4.2 Level Density

It has been established that the constant temperature and Bethe equations [21, 22, 23, 24] provide a good description of nuclear level densities. This study used the level density parameters of Gilbert and Cameron [21, 22] which were found to agree with the observed level structure, except in the case of $^{28}\mathrm{A}\ell$, where the level density of von Egidy [23] provided a substantially better agreement with the established structure. The effect of discrete levels was investigated by adding steps and discontinuities to the level density in order to more closely reproduce the observed level structure. Calculations using these discontinuous level density functions are referred to by the term "modified level density".

4.3 Reaction Cross Section Calculations

In calculating the reaction cross section in the compound nucleus formalism, both the compound nucleus formation probability and the channel decay probability are required. The level density parameterization used in this study makes no distinction between positive and negative parity states, and so the cross section, σ_J, for forming a compound nucleus of spin J from a target nucleus with spin $J_\circ$ is given by

$$\sigma_J = \sum_{l=|J-J_\circ|}^{J+J_\circ} \frac{2J+1}{(2J_\circ+1)(2l+1)} \sigma_c(l). \tag{1}$$

The channel decay probability is related to the probability of the reverse reaction through the principle of detailed balance. For a compound nucleus C with excitation energy E_0 and spin J that can decay into the residual nucleus B with excitation energy and spin E, J_1 and particle b with kinetic energy and total angular momentum ϵ, j, the channel decay probability $W_{b:JjJ_1}$ is

$$W_{b:JjJ_1} = \frac{2s_b+1}{2j+1} v_b \sigma_{C \leftarrow bB} \frac{\rho_i}{\rho_f}, \tag{2}$$

where for clarity the angular momentum labels for the cross section have been condensed into the particle labels C, b and B. In this case the term ρ_f is the density of states for the compound nucleus and ρ_i is the product of the density of states for the particle b and residual nucleus B, integrated under the restriction of energy conservation. The density of states for b is that of a free particle with velocity v_b, while for B it is the level density discussed previously. The transition probability is

$$W_{b:JjJ_1} = \frac{(2s_b+1)}{2j+1} \frac{m_b}{\pi^2\hbar^3} \frac{\rho_B(E)}{\rho_C(E_0)} \epsilon \sigma_{C \leftarrow Bb}\, dE, \tag{3}$$

which together with equation (1) provides the reaction cross section through a compound nuclear spin channel J,

$$\sigma_{Bb \leftarrow Aa} = \sigma_J \frac{\int_0^{E_R} dE \frac{(2s_b+1)}{(2j+1)} m_b \epsilon \sigma_{C \leftarrow Bb} \rho_B(E)}{\sum \int_0^{E'_R} dE \frac{(2s_{b'}+1)}{(2j'+1)} m_{b'} \epsilon \sigma_{C \leftarrow B'b'} \rho_{B'}(E)}, \tag{4}$$

where ϵ is the kinetic energy of the emitted particle b and m_b is its mass. In this equation the total decay probability has been normalized to unity to remove the dependence on the compound nucleus density of states. The integration occurs over the entire range of valid residual excitation energies between 0 and E_R, with $\epsilon = E_R - E$, while the normalization sums over all compound nucleus decay channels with spin J. The cross section into a residual nucleus excitation energy range between E_1 and E_2 was found by substituting these values for the integration limits 0 and E_R in the numerator of equation (4), and summing over all spin contributions (l, J, j and J_1) to this energy range.

In the parameterized and spin-independent calculations, only total absorption cross sections and level densities were used, and the total reaction cross section reduced to the same form of equation (4) without the dependence on j and j'. The upper limit of each integration was taken as the kinematic limit for each reaction product. Unrealistically large neutron cross sections at energies close to zero were avoided by adopting a low energy behavior described by

$$\sigma_n(\epsilon) = \sigma_n(\epsilon_{cut}) \left(\frac{\epsilon_{cut}}{\epsilon}\right)^{1/2} \tag{5}$$

below a suitable cut-off energy ϵ_{cut}. The sensitivity of the calculation to ϵ_{cut} was estimated by varying ϵ_{cut} in the calculation between 0.1 and 1 MeV, which produced changes in the calculated cross section on the order of 5%.

A large fraction of the α-particle absorption cross section occurs for high spin levels in the compound nucleus which are not experimentally observed [28]. Such high spin levels primarily contribute to the elastic scattering of the α-particle. This component of the cross section was removed by truncating the sum over J at the highest observed level spin near 8 MeV excitation in the compound nucleus, which is equivalent to restricting the sum over J to the first 5 or 6 lowest spins of the compound system.

The effects of the different data sources and approximations are illustrated in Fig. 2, which compares the published experimental total thick-target neutron yield [25, 26], for the $^{27}\mathrm{A}\ell(\alpha, n)$ reaction to calculated values. In the first level of approximation, the angular momentum coupling of the cross sections was ignored. Within this approximation, three different sets of cross sections were used: the parameterization of Chatterjee *et al.* [13], the results from optical calculations using the phenomenological potentials, and the optical calculation using the global potentials. Each of these cross section sets over-estimates the total thick-target neutron yield by as much as a factor of five. Introducing proper spin-coupling improved the overall agreement by almost 50% for both sets of optical potential cross sections, with approximately half the difference resulting from the restriction of the compound nuclear spin. These results are similar to those from the Hauser-Feshbach calculations of Woosley *et al.* [27], which differs primarily in its treatment of discrete levels. Both calculations reproduce the total neutron yield to within the same accuracy and agree with the experimental yield to within 50% over most of the energy range.

5 Theoretical Comparisons

Although the condition of overlapping compound nuclear states is met at the highest α-particle energy investigated, it is less clear whether the overlap is sufficient at lower energies to justify a simple statistical treatment of the reaction process. These calculations apply to the average behavior of the residual nucleus; as such, the experimental results to which these calculations are compared should sample many levels to reflect a configuration-averaged behavior. At low excitation energies, this average behavior is generally difficult to establish because of the low level density near the ground state.

The thick-target high energy nuclear excitation from 10 MeV α-particles, characterized by the level population distribution for residual nuclei of ^{28}Si, ^{29}Si and ^{30}Si is used to assess the level of agreement obtained when a large overlap of compound nuclear states exists. The theoretical and experimental population distributions dependence on α-particle energy are then examined for features which may signal the breakdown of statistical behavior and indicate a limitation to these calculations. Finally, theoretical and experimental direct production γ-ray distributions from α-particles are compared in order to assess the reliability with which theoretical calculations can be used in γ-ray background determinations.

5.1 Excitation of the Residual Nucleus

The direct population distribution for ^{28,29,30}Si was obtained using the measured yields in Tables 8, 10 and 13, respectively, and the known decay schemes to deduce the population of as many levels in the residual nucleus as possible. The results for $E_\alpha = 10$ MeV are shown in Fig. 3 summed into 1 MeV bins. The inclusion of allowed but unobserved levels would not significantly change the deduced distributions except where noted below.

The $E_\alpha = 10$ MeV population distribution for ^{28}Si is shown in Fig. 3(a). The $^{25}\mathrm{Mg}(\alpha, n)$ reaction populating this nucleus has one of the largest Q-values (2654 keV) of the reactions studied here, and correspondingly produced the highest energy excitation observed in a residual nucleus. This nucleus has only three excited states below 5 MeV. The absence of a nuclear level between 5 and 6 MeV gives rise to an empty bin in this energy range. The population of the other bins was fixed by three to six levels each. The largest number of unobserved levels occurred in the 9 to 10 MeV bin, and could increase this population by as much as a factor of two.

The measured population distribution for ^{29}Si is shown in Fig. 3(b). This nucleus contains five excited states below 4 MeV, two of which (between 3 and 4 MeV) decay through a γ-ray cascade below the energy cut-off of this study. As a result, no determination of the population distribution below 4 MeV could be made, and we have restricted our characterization to energies above this. The population distribution was determined from a sample of five levels in each of the 4 to 5 MeV and 6 to 7 MeV range, and two levels in each of the remaining

bins. The majority of undetermined level populations falls between 6 and 8 MeV, and could account for a factor of two increase in the 6 to 7 MeV population and a factor of 3 to 4 in the 7 to 8 MeV bin, assuming average populations for these levels.

The population distribution for ^{30}Si is shown in Fig. 3(c). This nucleus has six levels below 5 MeV, five of which decay primarily through the emission of γ-rays with energies of 2 MeV or greater. This nucleus contained the smallest number of undetermined level populations of those studied, and provided the most complete determination of the population distribution. Above an excitation of 5 MeV, the population in each bin was determined by at least 5 levels. The population of the 4 to 5 MeV bin was determined by only 2 levels. Levels with an undetermined population would increase no bin by more than 20% for an average estimated population.

In addition to the experimentally deduced population distribution, a set of statistical model calculations of the population distribution is shown in each figure. Each calculation, except for those using a modified level density, follows a smooth curve with excitation energy. Most calculations are well within a factor of two of the experimental measurements for these high energy excitations. Generally, the parameterized calculation predicts the largest populations. A somewhat better agreement with experiment was obtained in the spin-independent calculations by using global potential DWBA cross sections. A further improvement of about 15% occurred when spin coupling was properly accounted for. The modified level density calculation, employing the same cross sections reproduced some of the measured structure and generally achieved the best agreement with experimental results.

The results using the "phenomenological" potential DWBA calculations did not improve agreement with experiment. A larger variation of optical potential parameters with mass [16, 17] was anticipated for these light nuclei; this variation was expected to be followed more closely by experimental parameterizations of individual nuclei than by global potentials. However, the phenomenological potential calculations provided no improvement over the global potential ones, and in some cases were in considerably poorer agreement. In part this disagreement may have arisen from the extrapolation of the required optical potential parameters to unstable nuclei and different particle energies using the general trends established by the global potential, as well from inconsistencies between potential parameterizations of various research groups.

The calculations over-estimate the population distributions within 2 MeV of the maximum excitation energy. This is likely due to the compound-elastic component of the neutron and proton absorption cross sections. The compound-elastic component of the cross section can be ignored at incident energies where a large number of decay channels are available [28], but at low energies where only a few exit channels exist, this channel can account for a large fraction of the reaction cross section. In calculating the inverse reaction, these low incident energies correspond to the emission of low energy particles and consequently high energy excitations of the residual nucleus.

At low excitation energies, not shown in these figures, the statistical model calculations fall below the measured population by a factor of two to four. In part this under-estimate was corrected by the use of the modified level density in the calculation, which moved some strength to these lower energy regions. In most cases these low excitation energy populations were dominated by one or two levels, and as such were sensitive to non-statistical effects. As a result, these levels are considered to be inaccurately described by these calculations, and are not consider further.

5.2 Mean Excitation

The above discussion of the excitation distribution indicates an agreement between theory and measurement at $E_\alpha = 10$ MeV, with differences reflecting difficulties in the statistical characterization of experimental results rather than a breakdown in the theoretical model. In this section the behavior at lower α-particle energies is explored through the mean excitation energy of the residual nucleus.

The experimentally determined mean excitation curves for ^{28}Si, ^{29}Si and ^{30}Si in Fig. 4 were calculated from a population-weighted sum of the level energies. The theoretical mean was similarly obtained by treating the population of each bin as a single level at the bin center. Theoretical calculations exhibited a similar energy dependence largely independent of data source, and so only those using the global optical potential cross section are shown in Fig. 3.

Additional adjustments were required in the calculation of the experimental data mean. In order to avoid distortions, the populations of levels missing due to spectrum interference were excluded from the calculation. Low energy bins containing only one or two levels have been excluded through a low energy cut-off to avoid

non-statistical effects. Because of these adjustments, the calculations do not provide a true mean, but rather a sampling of the excitation which nevertheless should reflect the behavior of the true mean. Therefore, the comparison between theory and experiment focuses more on the slope rather than the absolute magnitude of the calculated mean. The adjusted uncertainty in the mean is due solely to statistical uncertainties.

The calculation of the mean excitation for ^{28}Si, shown in Fig. 4(b), utilized the measured excitations of levels above 5 MeV. The same level energy cut was used for the evaluation of the theoretical mean excitations. However, the selection of this energy cut has probably accentuated the effect of the discrete level structure by including an experimental bin in which no excitations are possible. The experimental points show a monotonically increasing mean excitation energy with α-particle energy. Levels with unknown populations can only significantly affect the $E_\alpha = 10$ and 8.8 MeV mean excitations, increasing the mean excitation energy by no more than 150 keV and 50 keV, respectively, for average populations of each level. Such an effect would not significantly change Fig. 4(b).

The behavior of the mean excitation energy is fairly well reproduced by the calculations. The calculation using the modified density shows a significantly higher mean energy due to the absence of an excitation in the 5 to 6 MeV bin, and is in significantly better agreement with experiment than calculations using a purely statistical level density. This illustrates the importance of using realistic level densities in such calculations. The slight deviation of the mean between $E_\alpha = 7$ and 7.7 MeV from a smooth behavior appears to be more likely caused by an uneven distribution of levels within the lowest energy bin than by a breakdown of the statistical nuclear model. Only three level were populated between 5 and 6 MeV, with two strongly populated levels near 6.9 MeV, and one near 6.3 MeV. At low α-particle energies, this bin accounts for most of the observed excitation and the distribution of levels could account for the observed behavior.

The behaviour of the mean excitation energy in ^{29}Si is shown in Fig. 4(c). Here, an energy cut of 4 MeV was used. The mean at $E_\alpha = 5.6$ MeV is not shown because only a single level was populated. All other points used at least 5 levels to determine the mean.

The experimental mean excitation exhibits a weaker dependence on E_α than that predicted by the calculations. This could indicate unobserved levels. For $E_\alpha = 10$ MeV, there are 14 levels between 6 and 8 MeV with unknown populations. Assigning an average excitation for these levels would increase the mean excitation energy at 10 MeV by 300 keV. Similarly, an unobserved population of levels close to the highest determined excitation in the 8.8 MeV run would significantly increase this mean excitation energy. These considerations indicate that the difference between the theoretical and experimental energy dependence cannot be attributed with certainty to a breakdown of the statistical model, and suggest that a more complete excitation measurement for this nucleus may indeed be consistent with the statistical compound nuclear model.

The mean excitation of ^{30}Si, shown in Fig. 4(c), used an energy cut of 5 MeV to avoid distortions from two strongly populated levels at 4809 and 4831 keV. The population of the 5231 keV level which is known only below $E_\alpha = 7.7$ MeV was excluded from the calculation of the mean excitation, to allow an appropriate comparison of run results.

A total of 8 undetermined level populations were excluded from the mean excitation energy determination at 10 MeV. At 7.7 and 8.8 MeV there were only 6 undetermined levels and below this energy only 3 levels had unknown excitations. In all cases the measured excitations comprised the majority of all known levels, and so provided a reasonable sample of the excitation of the ^{30}Si nucleus. Population of these missing levels would increase the measured results by less than 40 keV at all α-particle energies.

The theoretical calculations for ^{30}Si predicted an α-particle energy dependence which was consistent with experiment. Each calculation resulted in roughly the same slope and behavior, with somewhat shallower slopes being produced by the properly spin-coupled calculations.

5.3 α-Induced γ-Ray Yields from Materials

The statistical model has been used to generate γ-ray spectra resulting from α-particle irradiation within a composite material of light elements containing trace contaminations of uranium and thorium [30, 31]. The present calculations have also been used for this purpose, and provide a separate assessment of the accuracy of the statistical compound nuclear model for light elements. Such a comparison can be particularly useful in the understanding the nature of backgrounds in low background experiments.

Fig. 5 shows the calculated γ-ray spectrum for granite, a common host rock for several low-background laboratories, for a trace thorium mass fraction which is five times that of the uranium mass fraction. The

theoretical spectrum of Pomansky [29] for the direct production of γ-rays through the $(\alpha, n\gamma)$ and $(\alpha, p\gamma)$ reactions in granite is also shown, along with theoretical calculations using global potentials with full spin coupling. Both experimental and theoretical yields fall considerably below those reported by Pomansky using the calculations of Glotov [29, 30, 31].

The theoretical spectra from the present calculation also contained only $(\alpha, p\gamma)$ and $(\alpha, n\gamma)$ reaction yields. The excitation distribution for each residual nucleus was converted into a γ-ray spectrum by convolving these with the average γ-ray cascade from the known decay schemes of all the levels within each 1 MeV excitation bin. The calculation for bins corresponding to levels without known decay schemes were assumed to produce a single γ-ray by decay to the ground state. The spectrum for an individual element was constructed by adding together the individual γ-ray spectra, weighted by the target nucleus isotopic abundance. To obtain the full spectrum, the elemental contributions were then summed, weighted by their respective stopping powers as described in [1].

The theoretical γ-ray spectra calculations using global potentials, shown in Fig. 5, reproduce the gross shape of the spectrum constructed from the transition measurements of this study [1], and share similar overall features, except within 2 MeV of the maximum energy. The gross structure is largely determined by the excitation distribution of the residual nuclei, while departures from general trends are largely determined by details of the de-excitation γ-ray cascade. The spin-independent (not shown in Fig. 5) and fully spin coupled calculations produced similar spectra, with differences being less than 15%. The best agreement with measurement was obtained for the "global, modified density" calculation which used full spin-coupling, agreeing to within a factor of two over most of the γ-ray energy range. They also provide an order of magnitude improvement in agreement with measurement compared with the results of Pomansky and Glotov. This difference appears to arise from their use of experimental $^{25}\mathrm{Mg}(\alpha, n)$ yields [1, 30] to determine the $^{27}\mathrm{A}\ell(\alpha, p)$ and $^{23}\mathrm{Na}(\alpha, p)$ reaction rates. The calculation of these (α, p) reactions from (α, n) measurements require corrections for Coulomb barrier effects which are sensitive to spin-coupling. Also, Pomansky and Glotov made several simplifying approximations to produce conservative over-estimates of the γ-ray background.

6 Conclusions

We conclude that a simple calculation using the parameterized cross sections of Chatterjee *et al.* can predict the gross excitation population distribution of the residual nucleus to within a factor of two in the $A = 20$ to 30 mass region. A 50% improvement in the calculation can be obtained by using DWBA cross sections. Only a slight improvement is obtained by the proper treatment of spin-coupling, and no improvement in agreement with measured populations is obtained by using phenomenological potentials. We also find that it is important to use a level density which accurately reflects the low energy level structure of the residual nucleus. Such a treatment is most similar to Hauser-Feshbach calculations which have been used by a number of researchers to determine reaction rates in heavier nuclei than considered here. Such calculations by Woosley *et al.* (see Fig. 2) typically achieve agreement with measured yields within a factor of two, accuracy similar to that of our own calculations. A Hauser-Feshbach calculation for the reactions considered here could anticipate improvement due to a proper handling of level parities, and would be expected have a larger effect on the low energy populations, which tend to exhibit a parity bias, than at high energies. More significant improvements may be possible through a careful treatment of the compound-elastic component of the cross section. Such a calculation would be expected to significantly improve the agreement within 2 MeV of the maximum excitation energy.

No evidence for significant deviation in measured behavior from statistical model predictions has been found. All statistical model calculations produced similar mean excitation energy curves for each nucleus which was largely followed by the experimental measurements.

References

[1] R. K. Heaton, H. W. Lee, B. C. Robertson, E. B. Norman, K. T. Lesko and B. Sur, Nucl. Instrum. Methods in Phys. Res. **A364** 317 (1995).

[2] P. M. Endt, Nucl. Phys. **A310** 1 (1978).

[3] P. M. Endt, Nucl. Phys. **A521** 1 (1990).

[4] F. Ajzenberg-Selove, Nucl. Phys. **A475** 1 (1987).

[5] M. A. Lone, R. A. Leavitt and D. A. Harrison, At. Data Nucl. Data Tables **26** 511 (1981).

[6] R. K. Heaton, H. Lee, P. Skensved and B. C. Robertson, Nucl. Instrum. Methods in Phys. Res. **A276** 529 (1989).

[7] P. Dyer, D. Bodansky, D. D. Leach, E. B. Norman, and A. G. Seamster, Phys. Rev. **32** 1873 (1985).

[8] T. K. Alexander and J. S. Forster, Adv. Nucl. Phys. **10** 197 (1978).

[9] J. F. Ziegler, J. P. Biersack, and U. Littmack, *The Stopping and Ranges of Ions in Matter*, (Pergamon Press, New York, 1985).

[10] G. S. Mani., M. Melkanoff, I. Iore, CEA-2379 Report, 1963 (unpublished).

[11] J. R. Huizenga and G. J. Igo, Argonne National Laboratory Report ANL-6373, 1961 (unpublished).

[12] E. H. Auerbach and F. G. J. Perey, Brookhaven National Laboratory Report BNL-765 (T-286), 1962 (unpublished).

[13] A. Chatterjee, K. H. N. Murthy, and S. K. Gupta, Pramāna **16** 391 (1981).

[14] W. D. Hay and S. M. Perez, Nuclear Physics Theoretical Group Report # 42, Atlas Program Library Report # 15, Oxford University, 1969 (unpublished).

[15] C. M. Perey and F. G. Perey, At. Data Nucl. Data Tables **17** 1 (1976).

[16] F. D. Becchetti and G. W. Greenlees, Phys. Rev. **182** 1190 (1969).

[17] R. L. Varner, T. B. Clegg, T. L. McAbee, and W. J. Thompson, Phys. Lett. B **185** 6 (1987).

[18] J. M. Alexander, M. T. Magda and S. Landowne, Phys. Rev. C **42** 1092 (1990).

[19] F. G. Perey, Phys. Rev. **131**, 745 (1963).

[20] L. McFadden and G. R. Satchler, Nucl. Phys. **84** 177 (1966).

[21] A. Gilbert, F. S. Chen and A. G. W. Cameron, Can. J. Phys. **43** 1248 (1965).

[22] A. Gilbert and A. G. W. Cameron, Can. J. Phys. **43** 1446 (1965).

[23] T. von Egidy, A. N. Behkami and H. H. Schmidt, Nucl. Phys. **A454** 109 (1986).

[24] T. von Egidy, H. H. Schmidt and A. N. Behkami, Nucl. Phys. **A481** 189 (1988).

[25] D. West and A. C. Sherwood, Ann. Nucl. Energy **9** 551 (1982).

[26] R. Heaton, H. Lee, P. Skensved and B. C. Robertson, Nucl. Geophys. **4** 499 (1990).

[27] S. E. Woosley, W. A. Fowler, J. A. Holmes and B. Z. Zimmerman, Orange Aid Preprint OAP-422, California Institute of Technology, 1975.

[28] P. E. Hodgson, *Nuclear Reactions and Nuclear Structure*, (Clarendon Press, Oxford, 1971).

[29] A. A. Pomansky, Nucl. Instrum. Methods in Phys. Res. **B17** 406 (1986).

[30] V. I. Glotov, Ph.D. Dissertation (in Russian), Soviet Academy of Sciences, Institute of Nuclear Research, USSR, 1978.

[31] V. I. Glotov, translated from At. Energ. **30** 384 (1971).

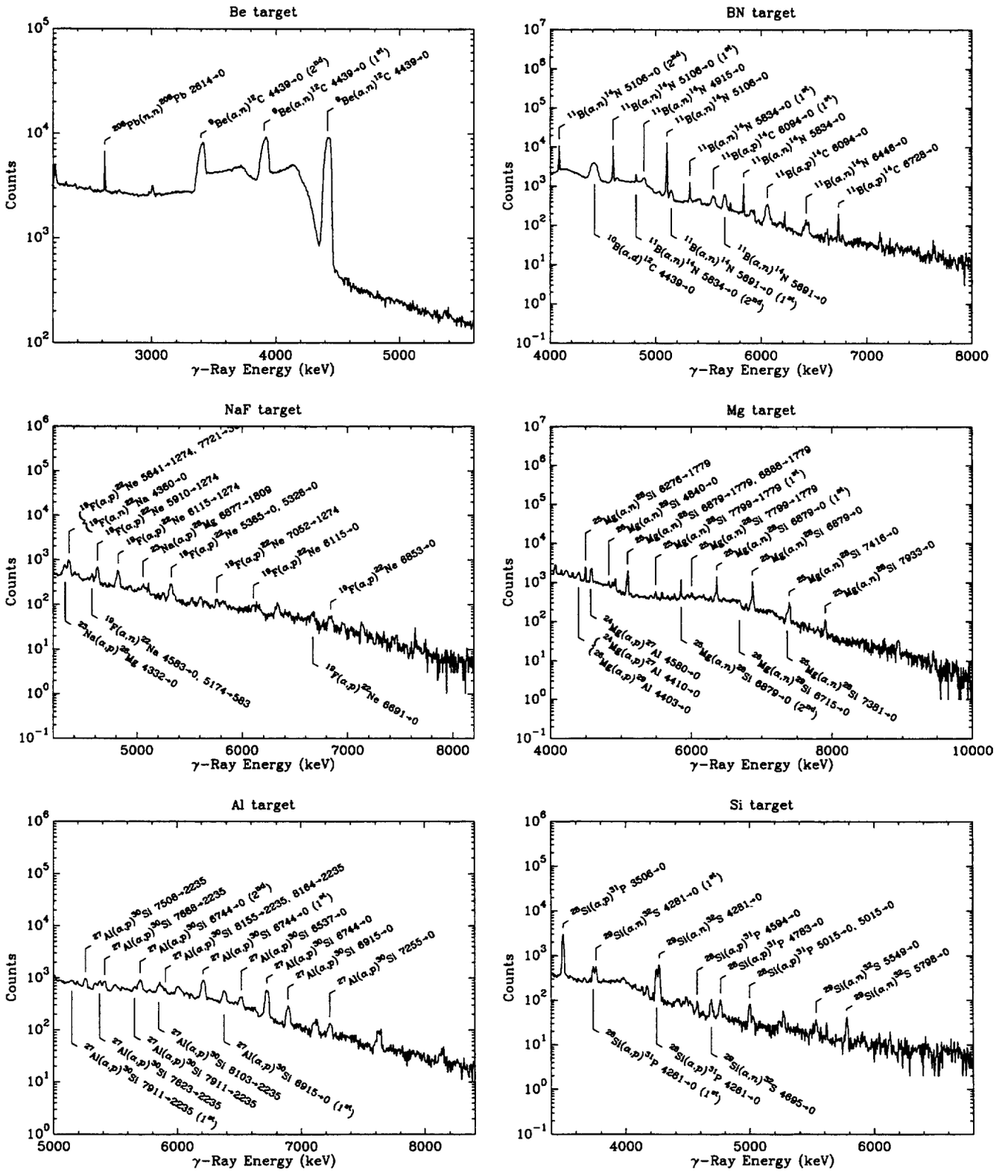

Figure 1: γ-ray spectra for $E_\alpha = 10$ MeV. Prominent peaks are labelled. Escape peaks have been indicated only in instances where they have been used in the yield calculation.

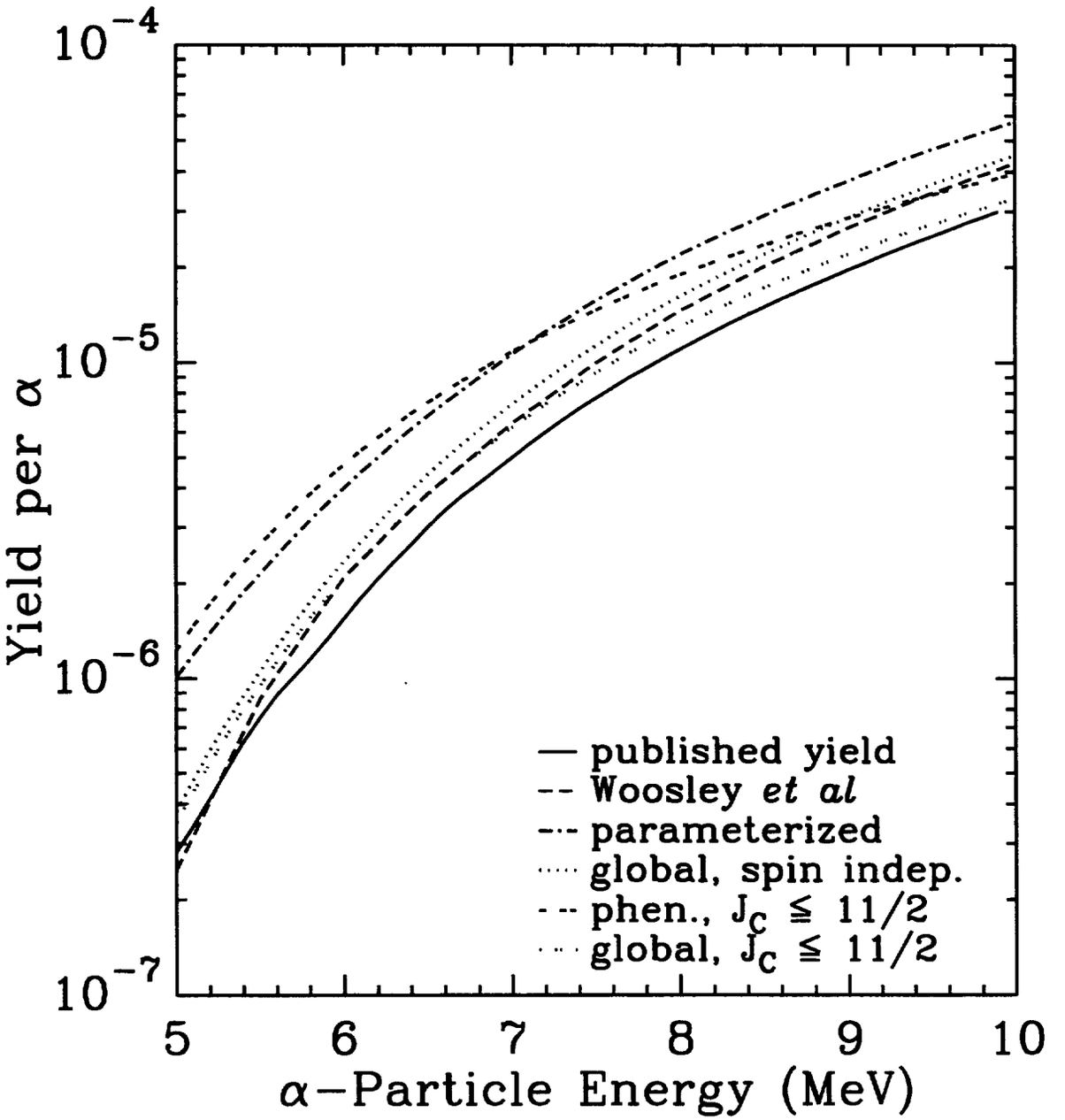

Figure 2: Theoretical ^{27}Aℓ thick-target neutron yields. The curve marked "published yields" indicates a composite of measured total neutron yields [25, 26].

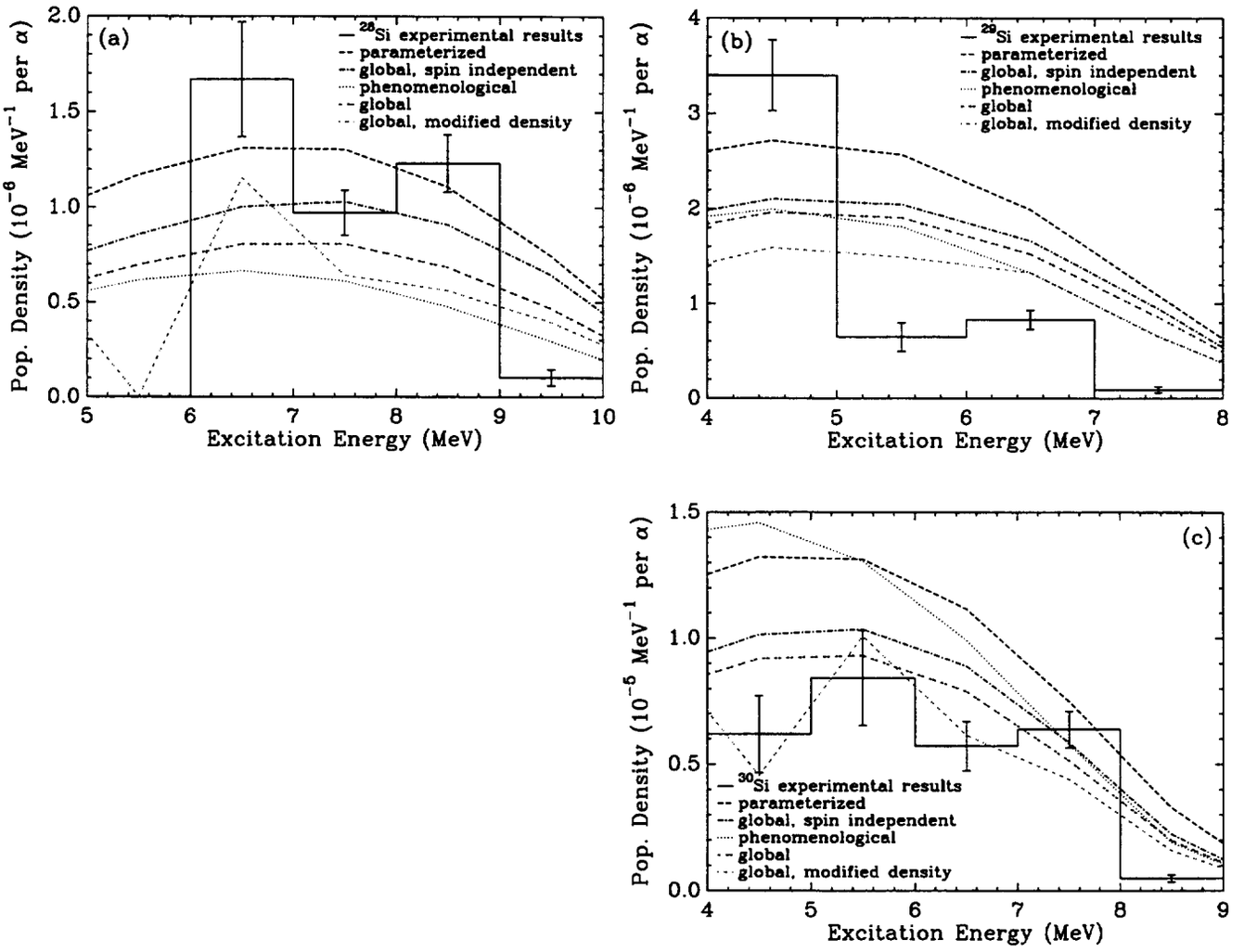

Figure 3: The $E_\alpha = 10$ MeV excitation population distribution of (a) ^{28}Si from the ^{25}Mg(α, n) reaction, (b) ^{29}Si from the ^{26}Mg(α, n) reaction and (c) ^{30}Si from the ^{27}A$\ell(\alpha, p)$ reaction. The deduced population distribution is shown by the histogram, with the error bars reflecting experimental uncertainties. The broken lines show the predicted populations from the statistical model, using the spin independent and spin-coupled calculations.

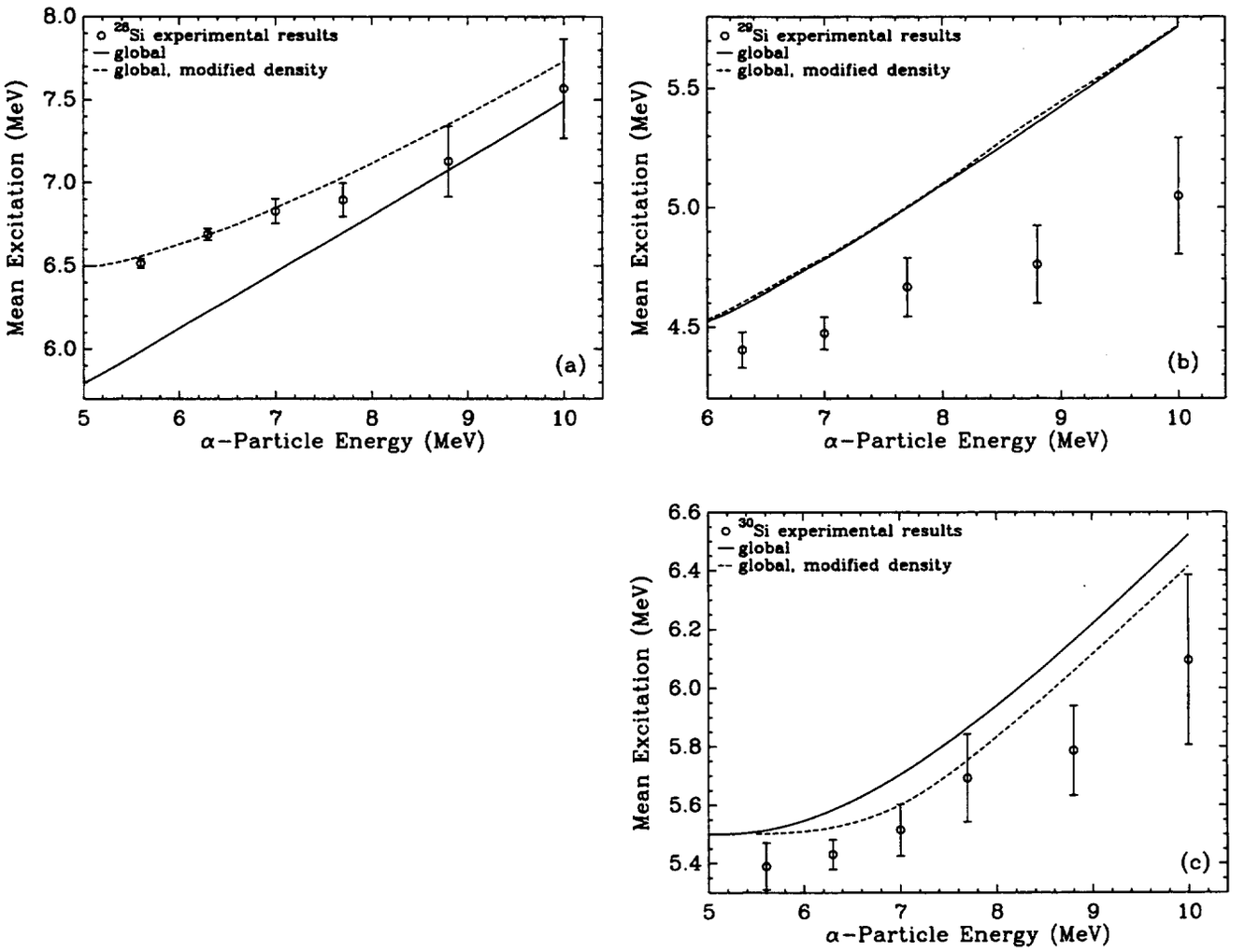

Figure 4: Mean excitation of (a) ^{28}Si from the ^{25}Mg(α, n) reaction, (b) ^{29}Si from the ^{26}Mg(α, n) reaction, and (c) ^{30}Si from the ^{27}A$\ell(\alpha, p)$ reaction.

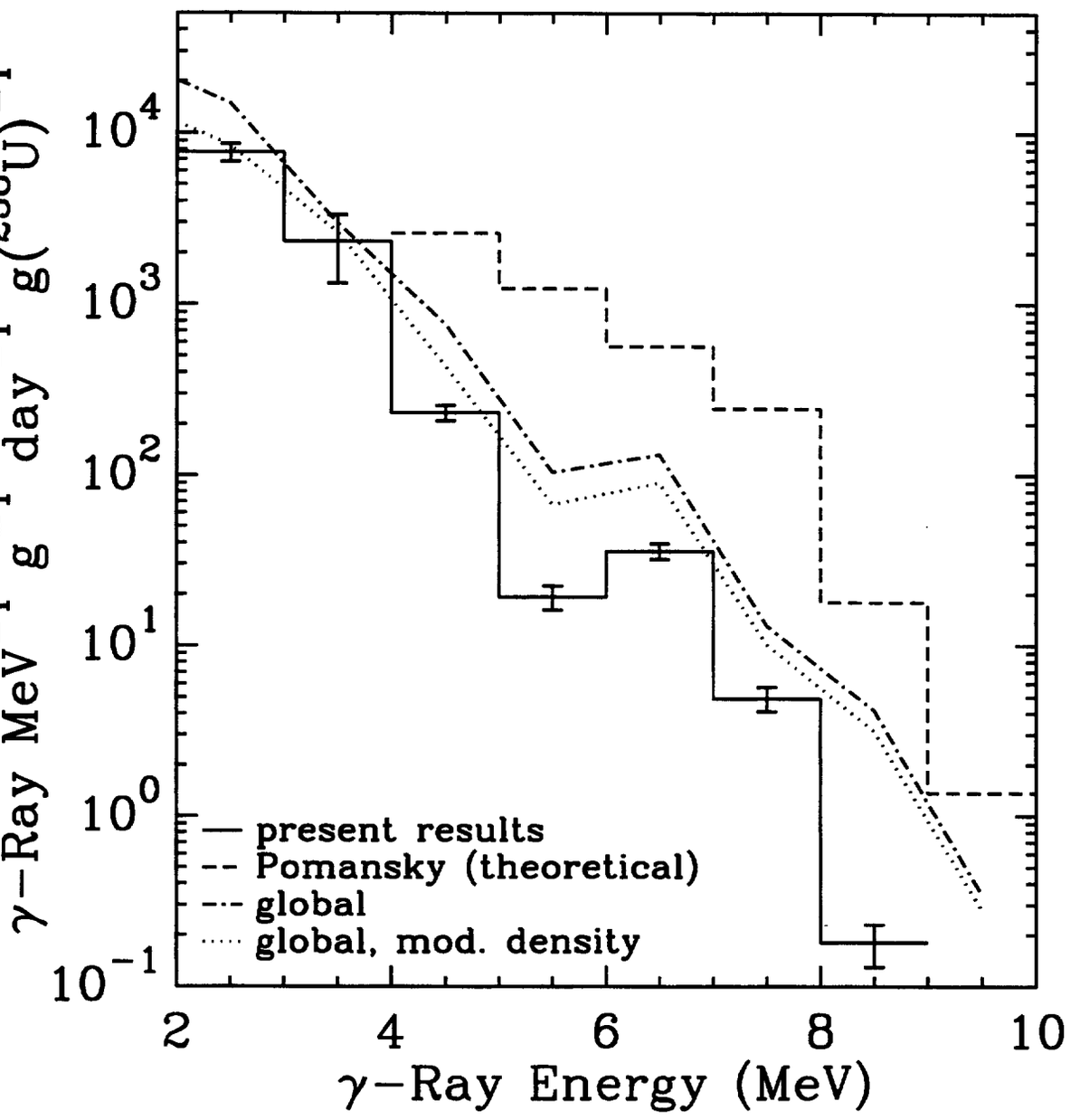

Figure 5: The direct α-induced γ-ray spectrum in granite. The solid curve labelled "present result" was constructed from measurements of the γ-ray The dotted and dot-dashed lines show the results of theoretical calculations using global potentials. The broken-line histogram shows the calculations of Pomansky.

Table 1: Thick-Target γ-Ray Yields from the $^{10}B(\alpha,p)^{13}C$ Reaction in Boron (quanta per α)

Transition (keV)		α-Particle Energy (MeV) 10.0	8.8	7.7	7.0	6.3	5.6
$3854 \rightarrow 0$	(3854)	$2.53 \pm 0.14(-6)$	$1.49 \pm 0.21(-6)$	$8.39 \pm 0.31(-7)$	$7.36 \pm 0.54(-7)$	$6.55 \pm 0.27(-7)$	$5.15 \pm 0.25(-7)$
$3684 \rightarrow 0$	(3684)	$6.90 \pm 0.29(-6)$	$4.12 \pm 0.57(-6)$	$2.71 \pm 0.13(-6)$	$2.26 \pm 0.16(-6)$	$2.01 \pm 0.09(-6)$	$1.39 \pm 0.07(-6)$
$3089 \rightarrow 0$	(3089)	$1.62 \pm 0.23(-6)$	$6.67 \pm 0.97(-7)$	$4.16 \pm 0.23(-7)$	$3.54 \pm 0.39(-7)$	$3.13 \pm 0.30(-7)$	$2.23 \pm 0.13(-7)$

Table 2: Thick-Target γ-Ray Yields from the $^{11}B(\alpha,n)^{14}N$ Reaction in Boron (quanta per α)

Transition (keV)		α-Particle Energy (MeV) 10.0	8.8	7.7	7.0	6.3	5.6
$6446 \rightarrow 0$	(6446)	$4.78 \pm 0.36(-7)$	—	—	—	—	—
$6203 \rightarrow 0$	(6203)	$1.31 \pm 0.36(-7)$	—	—	—	—	—
$5834 \rightarrow 0$	(5834)	$1.06 \pm 0.05(-6)$	—	—	—	—	—
$5691 \rightarrow 0$	(5691)	$9.64 \pm 0.63(-7)$	—	—	—	—	—
$5106 \rightarrow 0$	(5106)	$7.77 \pm 0.29(-6)$	$9.43 \pm 1.26(-7)$	$2.00 \pm 0.09(-7)$	—	—	—
$4915 \rightarrow 0$	(4915)	$1.43 \pm 0.12(-6)$	$3.06 \pm 0.52(-7)$	$9.54 \pm 1.00(-8)$	—	—	—
$3948 \rightarrow 0$	(3948)	$3.98 \pm 0.98(-7)$	$3.08 \pm 0.52(-7)$	$1.16 \pm 0.13(-7)$	$4.62 \pm 0.91(-8)$	$6.95 \pm 4.03(-9)$	—
$5691 \rightarrow 2313$	(3378)	$2.24 \pm 0.12(-6)$	—	—	—	—	—
$5106 \rightarrow 2313$	(2793)	$2.22 \pm 0.64(-6)^{\dagger}$	$2.39 \pm 0.38(-7)$	$4.69 \pm 0.80(-8)$	—	—	—
$6446 \rightarrow 3948$	(2498)	$9.22 \pm 3.55(-8)$	—	—	—	—	—
$2313 \rightarrow 0$	(2313)	$2.65 \pm 0.13(-5)$	$9.51 \pm 1.41(-6)$	$5.22 \pm 0.20(-6)$	$2.85 \pm 0.21(-6)$	$1.40 \pm 0.06(-6)$	$7.89 \pm 0.41(-7)$

†yield contains additional uncertainty from adjustment or contamination

Table 3: Thick-Target γ-Ray Yields per α from the $^{19}F(\alpha,n)^{22}Na$ Reaction (quanta per α)

Transition (keV)		α-Particle Energy (MeV) 10.0	8.8	7.7	7.0	6.3	5.6
$5101 \rightarrow 0$	(5101)	$1.63 \pm 0.79(-7)$	—	—	—	—	—
$5174 \rightarrow 583$	(4591)	$7.81 \pm 1.45(-7)$	—	—	—	—	—
$4583 \rightarrow 0$	(4583)						
$4360 \rightarrow 0^{\ddagger}$	(4360)	$2.54 \pm 0.68(-6)$	$3.69 \pm 0.95(-8)$	$1.10 \pm 0.40(-8)$	—	—	—
$5101 \rightarrow 891^{\ddagger}$	(4210)	$1.36 \pm 0.80(-7)$	—	—	—	—	—
$4622 \rightarrow 657^{\ddagger}$	(3965)	$6.10 \pm 3.18(-7)$	—	—	—	—	—
$4319 \rightarrow 657$	(3662)	$9.29 \pm 2.74(-7)$	—	—	—	—	—
$3519 \rightarrow 0^{\dagger}$	(3519)	$1.10 \pm 0.23(-6)$	$1.85 \pm 0.10(-7)$	$4.57 \pm 2.59(-8)$	—	—	—
$3943 \rightarrow 657$	(3286)	$2.03 \pm 0.26(-6)$	$2.48 \pm 0.53(-7)$	—	—	—	—
$4524 \rightarrow 1528^{\dagger}$	(2996)	$5.42 \pm 2.10(-6)$	$4.75 \pm 2.12(-7)$	—	—	—	—
$3707 \rightarrow 891$	(2816)	$4.61 \pm 0.36(-6)$	$3.56 \pm 0.68(-7)$	$1.23 \pm 0.25(-7)$	—	—	—
$4771 \rightarrow 1952$	(2819)						
$4622 \rightarrow 1952$	(2670)	$9.13 \pm 3.83(-7)$	—	—	—	—	—
$4583 \rightarrow 1952^{\dagger}$	(2631)	$6.03 \pm 6.32(-7)$	—	—	—	—	—
$2571 \rightarrow 0^{\dagger}$	(2571)	$6.43 \pm 2.01(-6)$	$2.72 \pm 0.68(-6)$	$1.48 \pm 0.34(-6)$	$6.14 \pm 1.74(-7)$	$3.29 \pm 0.80(-7)$	—
$4360 \rightarrow 1952$	(2408)	$1.08 \pm 0.21(-6)$	$1.56 \pm 0.36(-7)$	$4.66 \pm 1.50(-8)$	—	—	—
$4296 \rightarrow 1937$	(2359)	$1.34 \pm 0.67(-6)$	—	—	—	—	—
$3707 \rightarrow 1528^{\ddagger}$	(2179)	$6.98 \pm 5.32(-7)$	$1.67 \pm 0.36(-7)$	$5.80 \pm 1.30(-8)$	—	—	—

†yield contains additional uncertainty from adjustment or contamination
‡yield determined from deduced level population

Table 4: Thick-Target γ-Ray Yields from the $^{19}F(\alpha,p)^{22}Ne$ Reaction (quanta per α)

Transition (keV)		α-Particle Energy (MeV) 10.0	8.8	7.7	7.0	6.3	5.6
7489 → 0	(7489)	1.87 ± 0.55(−7)	—	—	—	—	—
7052 → 0	(7052)	9.43 ± 7.93(−8)	—	—	—	—	—
6853 → 0	(6853)	6.17 ± 0.96(−7)	—	—	—	—	—
6691 → 0	(6691)	3.94 ± 1.27(−7)	9.31 ± 2.01(−8)	—	—	—	—
7644 → 1274	(6369)	1.57 ± 1.06(−7)	—	—	—	—	—
7489 → 1274	(6214)	4.34 ± 0.82(−7)	—	—	—	—	—
6115 → 0	(6115)	4.61 ± 1.41(−7)	—	—	—	—	—
7052 → 1274	(5777)	4.79 ± 0.81(−7)	—	—	—	—	—
6904 → 1274	(5629)	1.64 ± 0.83(−7)	—	—	—	—	—
6817 → 1274	(5542)	3.40 ± 1.25(−7)	8.35 ± 3.34(−8)	—	—	—	—
5365 → 0	(5365)	3.87 ± 4.19(−7)	1.25 ± 1.09(−7)	5.17 ± 4.61(−7)	3.08 ± 1.55(−8)	1.20 ± 1.21(−8)‡	8.82 ± 9.05(−10)‡
5326 → 0	(5326)	1.61 ± 0.44(−6)	5.02 ± 1.72(−7)	1.93 ± 0.70(−7)	5.85 ± 3.47(−8)	2.34 ± 1.26(−8)	7.63 ± 1.98(−9)
6115 → 1274†	(4840)	1.87 ± 0.41(−6)	6.41 ± 1.62(−7)	1.50 ± 0.19(−7)	4.70 ± 1.36(−8)	1.27 ± 0.67(−8)	1.23 ± 1.67(−8)
5910 → 1274	(4635)	2.59 ± 0.20(−6)	6.64 ± 1.04(−7)	2.27 ± 0.22(−7)	5.83 ± 0.90(−8)	—	—
4457 → 0†	(4457)	3.82 ± 2.68(−7)	1.38 ± 1.10(−7)	7.42 ± 1.18(−8)	5.76 ± 2.28(−8)	1.62 ± 0.36(−8)	5.35 ± 1.27(−9)
5641 → 1274	(4367)	3.04 ± 0.93(−6)	8.80 ± 1.43(−7)	2.27 ± 0.53(−7)	1.18 ± 0.22(−7)	1.89 ± 0.36(−8)	2.21 ± 1.18(−9)
7721 → 3357‡	(4364)	2.59 ± 0.64(−6)	—	—	—	—	—
5365 → 1274	(4090)	3.49 ± 0.45(−6)	1.37 ± 0.20(−6)	5.92 ± 0.42(−7)	3.06 ± 0.29(−7)	1.10 ± 0.08(−7)	7.90 ± 1.55(−9)
5326 → 1274	(4052)	9.81 ± 7.97(−7)	2.68 ± 0.53(−7)	1.05 ± 0.16(−7)	3.06 ± 0.59(−8)	2.00 ± 0.43(−8)	3.22 ± 0.80(−9)
7341 → 3357	(3984)	4.59 ± 4.97(−7)	—	—	—	—	—
7721 → 4457	(3264)	5.85 ± 1.06(−7)	—	—	—	—	—
4457 → 1274 †	(3182)	1.00 ± 0.12(−5)	4.48 ± 0.72(−6)	2.68 ± 0.10(−6)	1.73 ± 0.15(−6)	8.73 ± 0.41(−7)	2.68 ± 0.13(−7)
6311 → 3357†	(2954)	3.67 ± 1.23(−6)	—	—	—	—	—
5910 → 3357‡	(2553)	1.85 ± 0.94(−7)	—	—	—	—	—
6817 → 4457‡	(2360)	2.17 ± 0.83(−7)	5.33 ± 2.22(−8)	—	—	—	—
5523 → 3357	(2166)	6.30 ± 2.15(−6)	1.62 ± 0.24(−6)	6.84 ± 0.45(−7)	2.65 ± 0.37(−7)	4.63 ± 1.07(−8)	—

†yield contains additional uncertainty from adjustment or contamination
‡yield determined from deduced level population

Table 5: Thick-Target γ-Ray Yields from the $^{23}Na(\alpha,n)^{26}A\ell$ Reaction (quanta per α)

Transition (keV)		α-Particle Energy (MeV) 10.0	8.8	7.7	7.0	6.3	5.6
3922 → 0	(3922)	8.42 ± 1.25(−7)	—	—	—	—	—
3508 → 0	(3508)	9.92 ± 1.85(−7)	1.16 ± 0.26(−7)	3.64 ± 2.09(−8)	—	—	—
3403 → 0	(3403)	6.59 ± 1.30(−7)	7.99 ± 2.09(−8)	—	—	—	—
3403 → 417‡	(2986)	1.02 ± 0.20(−6)	1.23 ± 0.30(−7)	—	—	—	—
2661 → 417	(2244)	8.37 ± 1.25(−7)	1.80 ± 0.42(−7)	—	—	—	—

‡yield determined from deduced level population

Table 6: Thick-Target γ-Ray Yields from the $^{23}Na(\alpha,p)^{26}Mg$ Reaction (quanta per α)

Transition (keV)		α-Particle Energy (MeV) 10.0	8.8	7.7	7.0	6.3	5.6
6877 → 1809	(5069)	4.41 ± 1.50(−7)	8.28 ± 2.07(−8)	—	—	—	—
6745 → 1809	(4936)	3.83 ± 0.87(−7)	3.87 ± 3.13(−8)	1.55 ± 0.53(−8)	—	—	—
4834 → 0 †	(4834)	—	—	2.95 ± 1.82(−8)	2.23 ± 1.30(−8)	1.10 ± 0.83(−8)	1.19 ± 1.76(−9)
4332 → 0	(4332)	5.49 ± 7.31(−7)	1.05 ± 0.30(−7)	7.06 ± 1.77(−8)	5.27 ± 1.01(−8)	2.39 ± 0.37(−8)	6.57 ± 1.73(−9)
7100 → 2938	(4162)	9.59 ± 1.70(−7)	—	—	—	—	—
6745 → 2938	(3807)	4.46 ± 1.16(−7)	—	—	—	—	—
6634 → 2938	(3696)	4.81 ± 1.68(−7)	6.77 ± 5.07(−8)	—	—	—	—
5474 → 1809	(3665)	5.51 ± 2.84(−7)	2.83 ± 0.59(−7)	7.69 ± 1.48(−8)	6.28 ± 1.01(−8)	—	—
4900 → 1809†	(3092)	3.87 ± 1.94(−6)	1.39 ± 0.34(−6)	7.02 ± 0.38(−7)	4.23 ± 0.35(−7)	1.24 ± 0.09(−7)	3.22 ± 0.33(−8)
4834 → 1809 †	(3026)	—	—	—	1.94 ± 1.22(−8)	7.65 ± 3.57(−9)	—
2938 → 0	(2938)	5.17 ± 0.74(−6)	6.59 ± 0.97(−7)	3.80 ± 0.38(−7)	2.88 ± 0.37(−7)	1.98 ± 0.13(−7)	9.16 ± 0.59(−8)
5715 → 2938 †	(2777)	2.57 ± 1.75(−7)	1.20 ± 0.43(−7)	6.95 ± 2.75(−8)	1.84 ± 0.85(−8)	—	—
5690 → 2938†	(2751)	9.94 ± 5.19(−7)	1.33 ± 0.41(−7)	6.39 ± 2.84(−8)	2.18 ± 1.42(−8)	—	—
4350 → 1809	(2541)						
4332 → 1809	(2524)	1.15 ± 0.07(−5)	4.68 ± 0.69(−6)	2.57 ± 0.25(−6)	1.87 ± 0.19(−6)	8.73 ± 0.47(−7)	3.51 ± 0.18(−7)
4318 → 1809	(2510)						
5291 → 2938	(2352)	1.44 ± 0.26(−6)	3.49 ± 0.60(−7)	1.89 ± 0.17(−7)	1.34 ± 0.36(−7)	3.73 ± 0.43(−8)	5.26 ± 1.88(−9)

†yield contains additional uncertainty from adjustment or contamination

Table 7: Thick-Target γ-Ray Yields from the $^{24}Mg(\alpha,p)^{27}A\ell$ Reaction (quanta per α)

Transition (keV)		α-Particle Energy (MeV) 10.0	8.8	7.7	7.0	6.3	5.6
5438 → 0	(5438)	4.20 ± 3.86(−8)	—	—	—	—	—
5156 → 0	(5156)	5.20 ± 1.83(−8)	—	—	—	—	—
4580 → 0	(4580)	4.42 ± 0.82(−7)	—	—	—	—	—
4410 → 0	(4410)	8.16 ± 5.42(−8)	6.32 ± 2.82(−8)	—	—	—	—
3957 → 0	(3957)	5.06 ± 0.87(−7)	—	—	—	—	—
4410 → 1014‡	(3396)	4.92 ± 3.26(−8)	7.31 ± 3.96(−9)	—	—	—	—
3957 → 844	(3113)	4.33 ± 1.53(−8)	—	—	—	—	—
3004 → 0	(3004)	3.72 ± 0.69(−6)	6.09 ± 0.86(−7)	2.92 ± 0.15(−7)	5.07 ± 0.62(−8)	1.03 ± 0.15(−8)	5.14 ± 0.83(−9)
2982 → 0†	(2982)	2.20 ± 0.60(−6)	5.81 ± 1.18(−7)	2.62 ± 0.14(−7)	1.98 ± 0.26(−8)	4.39 ± 0.92(−9)	2.10 ± 0.50(−9)
3957 → 1014	(2942)	5.68 ± 2.72(−8)	—	—	—	—	—
3680 → 844‡	(2837)	3.67 ± 1.51(−7)	5.66 ± 2.07(−8)	1.61 ± 1.23(−8)	—	—	—
2735 → 0	(2735)	1.03 ± 0.47(−6)	3.56 ± 0.54(−7)	1.20 ± 0.11(−7)	—	—	—
3680 → 1014	(2666)	2.27 ± 0.52(−7)	3.50 ± 1.35(−8)	9.94 ± 8.25(−9)	—	—	—
4580 → 2211	(2369)	1.12 ± 0.48(−7)	—	—	—	—	—
4510 → 2211	(2299)	8.07 ± 1.62(−7)	—	—	—	—	—
2211 → 0	(2211)	8.05 ± 1.42(−6)	2.60 ± 0.35(−6)	1.34 ± 0.06(−6)	3.61 ± 0.27(−7)	5.42 ± 0.63(−8)	1.47 ± 0.46(−8)

†yield contains additional uncertainty from adjustment or contamination
‡yield determined from deduced level population

Table 8: Thick-Target γ-Ray Yields from the $^{25}Mg(\alpha, n)^{28}Si$ Reaction (quanta per α)

Transition (keV)		α-Particle Energy (MeV) 10.0	8.8	7.7	7.0	6.3	5.6
9929 → 0	(9929)	9.62 ± 3.43(−9)	—	—	—	—	—
9796 → 0	(9796)	1.83 ± 0.92(−8)	—	—	—	—	—
9496 → 0	(9496)	4.45 ± 1.00(−8)	—	—	—	—	—
9479 → 0	(9479)						
8905 → 0	(8905)	3.28 ± 1.21(−8)	8.61 ± 2.97(−9)	—	—	—	—
8328 → 0	(8328)	3.36 ± 1.48(−8)	1.03 ± 0.22(−8)	5.45 ± 1.73(−9)	1.82 ± 0.91(−9)	—	—
8259 → 0	(8259)	2.10 ± 0.92(−8)	—	—	—	—	—
9796 → 1779	(8017)	1.59 ± 0.88(−8)	—	—	—	—	—
7933 → 0	(7933)	1.49 ± 0.29(−7)	5.90 ± 0.94(−8)	2.91 ± 0.27(−8)	1.16 ± 0.18(−8)	—	—
9382 → 1779	(7603)	5.53 ± 3.62(−8)	—	—	—	—	—
7416 → 0	(7416)	2.73 ± 0.71(−7)	1.19 ± 0.22(−7)	6.11 ± 0.70(−8)	3.68 ± 0.47(−8)	1.26 ± 0.10(−8)	—
7381 → 0	(7381)	1.10 ± 0.99(−7)	4.43 ± 1.12(−8)	1.83 ± 0.29(−8)	8.13 ± 1.24(−9)	3.38 ± 0.62(−9)	—
6879 → 0	(6879)	5.39 ± 0.93(−7)	2.49 ± 0.36(−7)	1.38 ± 0.09(−7)	7.58 ± 0.51(−8)	3.36 ± 0.22(−8)	5.97 ± 0.42(−9)
8589 → 1779	(6810)	9.06 ± 2.15(−8)	2.18 ± 0.72(−8)	6.00 ± 3.54(−9)	—	—	—
8413 → 1779	(6634)	1.51 ± 0.31(−7)	2.28 ± 1.06(−8)	—	—	—	—
8259 → 1779	(6480)	8.57 ± 2.91(−8)	3.17 ± 0.71(−8)	—	—	—	—
7799 → 1779	(6020)	1.74 ± 0.36(−7)	6.56 ± 1.08(−8)	2.28 ± 0.60(−8)	1.44 ± 0.30(−8)	—	—
7381 → 1779	(5602)	1.51 ± 0.43(−7)	6.26 ± 1.08(−8)	3.47 ± 0.31(−8)	2.21 ± 0.22(−8)	5.22 ± 0.68(−9)	—
6888 → 1779	(5109)	7.79 ± 1.40(−7)	3.92 ± 0.55(−7)	2.05 ± 0.10(−7)	1.24 ± 0.09(−7)	7.06 ± 0.44(−8)	1.32 ± 0.09(−8)
6879 → 1779	(5100)	2.10 ± 0.61(−7)	9.72 ± 2.30(−7)	5.37 ± 0.75(−8)	2.96 ± 0.44(−8)	1.31 ± 0.22(−8)	2.33 ± 0.65(−9)
6276 → 1779	(4497)	6.11 ± 1.07(−7)	3.88 ± 0.54(−7)	2.22 ± 0.10(−7)	1.56 ± 0.11(−7)	8.36 ± 0.50(−8)	2.97 ± 0.18(−8)
8945 → 4618	(4327)	1.16 ± 0.24(−7)	—	—	—	—	—
8413 → 4618‡	(3795)	1.89 ± 0.41(−8)	—	—	—	—	—
4980 → 1779	(3201)	4.22 ± 0.76(−7)	1.17 ± 0.18(−7)	6.44 ± 0.38(−8)	4.42 ± 0.39(−8)	3.41 ± 0.22(−8)	1.62 ± 0.11(−8)
4618 → 1779	(2839)	2.21 ± 0.39(−6)	1.20 ± 0.17(−6)	6.49 ± 0.35(−7)	4.58 ± 0.31(−7)	2.94 ± 0.17(−7)	1.43 ± 0.08(−7)

‡yield determined from deduced level population

Table 9: Thick-Target γ-Ray Yields from the $^{25}Mg(\alpha, p)^{28}A\ell$ Reaction (quanta per α)

Transition (keV)		α-Particle Energy (MeV) 10.0	8.8	7.7	7.0	6.3	5.6
3591 → 0	(3591)	3.71 ± 1.53(−8)	2.07 ± 2.31(−8)	—	—	—	—
3465 → 0	(3465)	1.11 ± 0.27(−7)	—	—	—	—	—
3347 → 0	(3347)	1.11 ± 0.26(−7)	2.59 ± 0.90(−8)	1.62 ± 0.43(−8)	—	—	—
2272 → 0	(2272)	4.06 ± 0.88(−7)	1.29 ± 0.20(−7)	6.20 ± 0.79(−8)	3.10 ± 0.46(−8)	1.37 ± 0.55(−8)	—
2201 → 31 †	(2171)	—	1.66 ± 1.06(−8)	2.46 ± 2.15(−8)	—	—	—
2139 → 0	(2139)	5.69 ± 2.78(−8)	3.66 ± 1.23(−8)	1.64 ± 0.69(−8)	9.63 ± 3.99(−9)	8.04 ± 4.33(−9)	—
2139 → 31	(2108)	1.69 ± 0.78(−7)	4.76 ± 1.96(−8)	1.81 ± 0.40(−8)	1.25 ± 0.39(−8)	6.28 ± 3.68(−9)	—

†yield contains additional uncertainty from adjustment or contamination

Table 10: Thick-Target γ-Ray Yields from the $^{26}Mg(\alpha,n)^{29}Si$ Reaction (quanta per α)

Transition (keV)		α-Particle Energy (MeV) 10.0	8.8	7.7	7.0	6.3	5.6
7692 → 0	(7692)	2.73 ± 1.50(−8)	—	—	—	—	—
6715 → 0	(6715)	1.50 ± 0.36(−7)	—	—	—	—	—
6522 → 1273	(5249)	3.52 ± 1.30(−8)	—	—	—	—	—
7072 → 2028	(5044)	6.19 ± 2.74(−8)	—	—	—	—	—
4935 → 0	(4935)	3.16 ± 0.92(−7)	1.47 ± 0.27(−7)	7.21 ± 0.75(−8)	3.34 ± 0.48(−8)	1.02 ± 0.13(−8)	—
4895 → 0	(4895)	1.54 ± 0.46(−7)	7.59 ± 1.51(−8)	4.52 ± 0.84(−8)	2.07 ± 0.36(−8)	1.17 ± 0.13(−8)	—
4840 → 0	(4840)	1.39 ± 0.34(−7)	1.21 ± 0.19(−7)	4.99 ± 0.45(−8)	2.94 ± 0.27(−8)	5.81 ± 1.26(−9)	—
5949 → 1273	(4676)	4.25 ± 2.52(−8)	1.64 ± 0.99(−8)	9.95 ± 4.01(−9)	—	—	—
6194 → 2028	(4166)	1.91 ± 0.46(−7)	3.97 ± 1.07(−8)	—	—	—	—
6522 → 2426‡	(4096)	2.69 ± 1.01(−8)	—	—	—	—	—
6107 → 2028	(4079)	1.39 ± 0.37(−7)	5.02 ± 1.61(−8)	—	—	—	—
5813 → 2028	(3785)	1.10 ± 0.30(−7)	3.15 ± 0.77(−8)	1.39 ± 0.29(−8)	—	—	—
6107 → 2426‡	(3681)	6.63 ± 1.81(−8)	2.84 ± 1.65(−8)	—	—	—	—
4895 → 1273	(3622)	2.49 ± 0.45(−7)	1.13 ± 0.30(−7)	5.63 ± 0.33(−8)	2.33 ± 0.27(−8)	9.59 ± 0.87(−9)	—
4840 → 1273†	(3567)	—	2.26 ± 0.86(−8)	1.09 ± 0.27(−8)	6.73 ± 2.49(−9)	—	—
5949 → 2426	(3523)	5.14 ± 4.06(−8)	1.08 ± 0.66(−8)	9.47 ± 4.50(−9)	—	—	—
5813 → 2426	(3387)	1.19 ± 0.45(−7)	1.86 ± 1.56(−8)	1.22 ± 0.39(−8)	—	—	—
6781 → 3624	(3157)	6.74 ± 1.81(−8)	—	—	—	—	—
5949 → 3067 ‡	(2882)	5.05 ± 2.59(−8)	1.59 ± 0.73(−8)	1.15 ± 0.37(−8)	—	—	—
4895 → 2028 ‡	(2867)	8.84 ± 1.92(−8)	5.11 ± 1.18(−8)	2.00 ± 0.26(−8)	—	—	—
4080 → 1273	(2807)	7.61 ± 1.56(−7)	3.26 ± 0.47(−7)	1.49 ± 0.15(−7)	8.59 ± 0.66(−8)	3.54 ± 0.32(−8)	5.88 ± 0.46(−9)
5813 → 3067	(2746)	2.29 ± 0.61(−7)‡	7.25 ± 3.20(−8)	2.67 ± 1.58(−8)	—	—	—
4741 → 2028	(2713)	9.32 ± 1.72(−7)	2.69 ± 0.39(−7)	1.49 ± 0.10(−7)	6.94 ± 0.62(−8)	2.10 ± 0.23(−8)	—
2426 → 0	(2426)	1.30 ± 0.21(−6)	7.68 ± 1.07(−7)	4.56 ± 0.26(−7)	3.27 ± 0.23(−7)	2.28 ± 0.13(−7)	1.19 ± 0.07(−7)

†yield contains additional uncertainty from adjustment or contamination
‡yield determined from deduced level population

Table 11: Thick-Target γ-Ray Yields from the $^{26}Mg(\alpha,p)^{29}A\ell$ Reaction (quanta per α)

Transition (keV)		α-Particle Energy (MeV) 10.0	8.8	7.7	7.0	6.3	5.6
4403 → 0	(4403)	2.40 ± 0.77(−7)	—	—	—	—	—
3641 → 0 †	(3641)	—	1.72 ± 1.20(−8)	—	—	—	—
2866 → 0†	(2866)	2.16 ± 1.43(−7)	1.11 ± 0.54(−7)	4.52 ± 2.13(−8)†	1.17 ± 2.71(−8)	—	—

†yield contains additional uncertainty from adjustment or contamination

Table 12: Thick-Target γ-Ray Yields from the $^{27}A\ell(\alpha,n)^{30}P$ Reaction (quanta per α)

Transition (keV)		α-Particle Energy (MeV) 10.0	8.8	7.7	7.0	6.3	5.6
5208 → 0	(5208)	4.33 ± 1.44(−8)	—	—	—	—	—
5208 → 709	(4499)	2.17 ± 1.69(−8)	—	—	—	—	—
4144 → 0	(4144)	4.01 ± 0.92(−7)	—	—	—	—	—
3734 → 0	(3734)	1.86 ± 0.60(−6)	—	—	—	—	—
3734 → 677	(3057)	1.37 ± 0.85(−6)	—	—	—	—	—
2938 → 0	(2938)	2.34 ± 0.55(−7)	4.72 ± 1.75(−8)	2.23 ± 0.98(−8)	4.04 ± 2.98(−9)	—	—
2840 → 0	(2840)	4.52 ± 0.98(−7)	1.33 ± 0.39(−7)	7.31 ± 1.95(−8)	—	—	—
2724 → 0	(2724)	1.73 ± 0.34(−6)	6.48 ± 1.09(−7)	2.84 ± 0.20(−7)	6.61 ± 2.10(−8)	—	—
2539 → 0†	(2539)	4.04 ± 0.85(−6)	1.23 ± 0.19(−6)	6.79 ± 0.72(−7)	1.82 ± 0.31(−7)	—	—
3929 → 1455	(2474)	2.51 ± 1.02(−7)	—	—	—	—	—
3019 → 677	(2342)	8.73 ± 1.88(−7)	2.11 ± 0.68(−7)	9.61 ± 2.15(−8)	1.26 ± 1.41(−8)	—	—
3734 → 1455	(2279)	6.03 ± 2.21(−7)	—	—	—	—	—
2938 → 677	(2261)	5.51 ± 2.57(−7)	—	—	—	—	—
2840 → 709	(2131)	1.23 ± 0.24(−6)	3.85 ± 1.22(−7) ‡	1.31 ± 0.37(−7)	4.55 ± 1.73(−8)	—	—

†yield contains additional uncertainty from adjustment or contamination
‡yield determined from deduced level population

Table 13: Thick-Target γ-Ray Yields from the $^{27}A\ell(\alpha,p)^{30}Si$ Reaction (quanta per α)

Transition (keV)		α-Particle Energy (MeV) 10.0	8.8	7.7	7.0	6.3	5.6
8164 → 0	(8164)	2.99 ± 0.72(−8)	—	—	—	—	—
7623 → 0 †	(7623)	2.23 ± 1.00(−8)	3.74 ± 1.54(−9)	—	—	—	—
7255 → 0	(7255)	6.51 ± 1.38(−8)	1.15 ± 0.24(−8)	4.55 ± 1.17(−9)	—	—	—
6915 → 0	(6915)	1.85 ± 0.35(−7)	3.65 ± 0.53(−8)	1.43 ± 0.14(−8)	2.85 ± 0.47(−9)	—	—
6744 → 0	(6744)	3.64 ± 0.64(−7)	1.26 ± 0.18(−7)	5.20 ± 0.31(−8)	9.95 ± 1.03(−9)	—	—
6537 → 0	(6537)	1.35 ± 0.25(−7)	5.49 ± 0.78(−8)	2.41 ± 0.17(−8)	4.92 ± 0.61(−9)	—	—
8330 → 2235	(6095)	3.72 ± 1.35(−8)	—	—	—	—	—
8290 → 2235	(6055)	5.48 ± 2.24(−8)	—	—	—	—	—
8164 → 2235	(5929)	4.25 ± 1.34(−8)	—	—	—	—	—
8155 → 2235	(5920)						
8103 → 2235	(5868)	8.85 ± 2.73(−8)	—	—	—	—	—
7911 → 2235	(5676)	6.98 ± 1.58(−8)	—	—	—	—	—
7668 → 2235	(5433)	1.50 ± 0.30(−7)	1.73 ± 0.81(−8)	—	—	—	—
7623 → 2235	(5388)	1.16 ± 0.25(−7)	1.83 ± 0.89(−8)	—	—	—	—
7508 → 2235	(5273)	1.59 ± 0.30(−7)	1.75 ± 0.38(−8)	5.13 ± 1.30(−9)	—	—	—
7255 → 2235	(5020)	7.48 ± 1.72(−8)	1.14 ± 0.45(−8)	2.67 ± 1.19(−9)	—	—	—
7079 → 2235	(4844)	2.28 ± 0.49(−7)	5.76 ± 1.41(−8)	2.05 ± 0.61(−8)	—	—	—
4809 → 0	(4809)	1.03 ± 0.18(−6)	5.24 ± 0.72(−7)	3.03 ± 0.16(−7)	1.87 ± 0.22(−7)	1.07 ± 0.05(−7)	4.07 ± 0.21(−8)
8190 → 3498	(4692)	5.48 ± 8.70(−8)	—	—	—	—	—
6915 → 2235	(4680)	2.60 ± 1.07(−7)	4.92 ± 1.48(−8)	1.82 ± 0.28(−8)	3.59 ± 1.31(−9)	—	—
6865 → 2235	(4630)	4.54 ± 0.97(−7)	1.42 ± 0.25(−7)	4.43 ± 0.59(−8)	7.34 ± 2.14(−9)	—	—
7911 → 3498 ‡	(4413)	1.72 ± 0.68(−8)	—	—	—	—	—
6641 → 2235	(4406)	6.25 ± 0.97(−7)	1.54 ± 0.21(−7)	7.65 ± 0.48(−8)	1.32 ± 0.15(−8)	1.32 ± 1.59(−9)	—
7668 → 3498 ‡	(4170)	3.45 ± 1.17(−8)	—	—	—	—	—
7623 → 3498 ‡	(4125)	1.89 ± 0.57(−8)	—	—	—	—	—
3769 → 0	(3769)	1.17 ± 0.20(−6)	7.26 ± 1.10(−7)	4.00 ± 0.33(−7)	1.71 ± 0.37(−7)	1.11 ± 0.09(−7)	3.70 ± 0.38(−8)
7255 → 3498	(3757)	5.48 ± 1.77(−7)	—	—	—	—	—
5951 → 2235	(3716)	2.31 ± 0.68(−6)	1.50 ± 0.23(−6)	6.72 ± 0.40(−7)	2.23 ± 0.20(−7)	5.98 ± 0.37(−8)	6.57 ± 1.26(−9)
7079 → 3498	(3581)	1.69 ± 0.55(−7)	1.69 ± 1.08(−8)	—	—	—	—
3498 → 0	(3498)	6.07 ± 1.06(−6)	3.02 ± 0.41(−6)	1.67 ± 0.09(−6)	9.40 ± 0.81(−7)	5.52 ± 0.28(−7)	2.43 ± 0.11(−7)
5614 → 2235	(3379)	4.98 ± 1.05(−7)	2.69 ± 0.60(−7)	1.36 ± 0.17(−7)	6.22 ± 1.39(−8)	2.61 ± 0.59(−8)	5.64 ± 2.86(−9)
5487 → 2235	(3252)	2.33 ± 0.42(−6)	1.09 ± 0.15(−6)	5.69 ± 0.44(−7)	3.34 ± 0.54(−7)	1.41 ± 0.11(−7)	3.81 ± 0.65(−8)
6915 → 3769‡	(3146)	5.21 ± 2.20(−8)	1.01 ± 0.41(−8)	3.83 ± 1.48(−9)	7.73 ± 3.16(−10)	—	—
5372 → 2235	(3137)	1.08 ± 0.44(−7)	8.24 ± 3.17(−8)	3.41 ± 0.85(−8)	1.98 ± 0.64(−8)	1.07 ± 0.47(−8)	—
5280 → 2235	(3045)	4.94 ± 1.00(−6)	2.64 ± 0.37(−6)	1.40 ± 0.10(−6)	8.17 ± 0.73(−7)	4.02 ± 0.22(−7)	1.26 ± 0.08(−7)
6537 → 3498‡	(3039)	4.32 ± 1.22(−6)	1.77 ± 0.91(−7)	7.81 ± 2.02(−8)	—	—	—
5231 → 2235	(2996)	4.10 ± 1.46(−6)	7.38 ± 2.57(−7)	2.65 ± 0.86(−7)	6.42 ± 1.63(−8)	3.44 ± 0.73(−8)	1.12 ± 0.87(−8)
4831 → 2235	(2596)	5.37 ± 0.96(−6)	2.28 ± 0.32(−6)	1.46 ± 0.12(−6)	7.17 ± 0.65(−7)	3.15 ± 0.20(−7)	1.32 ± 0.11(−7)
4809 → 2235‡	(2574)	4.51 ± 1.01(−7)	2.23 ± 0.46(−7)	1.29 ± 0.21(−7)	7.94 ± 1.47(−8)	4.56 ± 0.74(−8)	1.73 ± 0.29(−8)
5951 → 3498	(2453)	1.84 ± 0.74(−7)	—	—	—	—	—
7255 → 4809	(2446)						
7079 → 4809‡	(2270)	1.90 ± 0.32(−7)	—	—	—	—	—
2235 → 0	(2235)	4.89 ± 0.86(−5)	2.02 ± 0.28(−5)	1.11 ± 0.06(−5)	6.37 ± 0.56(−6)	3.39 ± 0.17(−6)	1.52 ± 0.07(−6)
7001 → 4831	(2170)	3.56 ± 0.75(−7)	7.29 ± 1.58(−8)	2.15 ± 0.82(−8)	—	—	—

†yield contains additional uncertainty from adjustment or contamination
‡yield determined from deduced level population

Table 14: 10 MeV Thick-Target γ-Ray Yields from Silicon (quanta per α)

Transition (keV)		Yields	Transition (keV)		Yields
		^{28}Si$(\alpha,p)^{31}$P:			
5256 → 0	(5256)	$6.86 \pm 1.97(-9)$	5015.4 → 0 5015.2 → 0	(5015) (5015)	$2.29 \pm 0.26(-8)$
4783 → 0	(4783)	$2.42 \pm 0.32(-8)$	4594 → 0	(4594)	$1.45 \pm 0.67(-8)$
4261 → 0	(4261)	$1.46 \pm 0.09(-7)$	3506 → 0	(3506)	$7.48 \pm 0.28(-7)$
4594 → 1266	(3327)	$2.92 \pm 0.72(-8)$	5529 → 2234	(3296)	$1.81 \pm 0.64(-8)$
3134 → 0	(3134)	$5.45 \pm 0.22(-7)$	4261 → 1266	(2995)	$6.89 \pm 1.62(-8)$
4634 → 2234	(2400)	$2.44 \pm 0.66(-7)$	3506 → 1266 ‡	(2240)	$5.20 \pm 0.36(-7)$
2234 → 0	(2234)	$1.04 \pm 0.21(-5)$	4431 → 2234	(2197)	$1.69 \pm 0.21(-7)$
3415 → 1266	(2148)	$3.34 \pm 0.69(-6)$			
		^{29}Si$(\alpha,n)^{32}$S:			
5798 → 0	(5798)	$1.41 \pm 0.22(-8)$	5549 → 0	(5549)	$1.09 \pm 0.23(-8)$
4695 → 0	(4695)	$2.88 \pm 0.39(-8)$	4281 → 0	(4281)	$1.90 \pm 0.09(-7)$
5549 → 2230	(3319)	$1.54 \pm 0.92(-8)$	5413 → 2230	(3183)	$6.26 \pm 0.67(-8)$
5006 → 2230	(2776)	$1.25 \pm 0.14(-7)$	4695 → 2230	(2465)	$3.23 \pm 1.62(-8)$
		^{29}Si$(\alpha,p)^{32}$P:			
4149 → 78	(4071)	$7.02 \pm 4.83(-9)$	3793 → 78	(3715)	$9.12 \pm 4.02(-9)$
3320 → 78	(3242)	$7.78 \pm 1.73(-8)$	3005 → 0	(3005)	$3.26 \pm 1.61(-8)$
3005 → 78	(2927)	$1.82 \pm 0.40(-7)$	3793 → 1323	(2470)	$1.24 \pm 1.39(-8)$
		^{30}Si$(\alpha,n)^{33}$S:			
4144 → 0	(4144)	$1.64 \pm 0.53(-8)$	3832 → 0	(3832)	$1.12 \pm 0.42(-8)$
4211 → 841	(3370)	$1.74 \pm 0.62(-8)$	3221 → 0‡	(3221)	$1.78 \pm 0.76(-8)$
2969 → 0	(2969)	$2.04 \pm 0.32(-7)$	2935 → 0	(2935)	$1.13 \pm 0.48(-7)$
2868 → 0	(2868)	$9.92 \pm 1.84(-8)$	3221 → 841	(2380)	$3.11 \pm 1.39(-8)$
2313 → 0	(2313)	$7.05 \pm 2.20(-8)$			
		^{30}Si$(\alpha,p)^{33}$P:			
4194 → 0	(4194)	$1.49 \pm 0.41(-8)$			

‡yield determined from deduced level population